Image processing methods for limited angle tomography and sparse angle tomography

Martti Kalke

Academic dissertation

To be presented, with the permission of the Faculty of Science of the University of Helsinki, for public examination in the Auditorium D101 of Physicum building at Kumpula campus on November 21st, 2014, at 12 o'clock noon.

Department of Mathematics and Statistics
Faculty of Science
University of Helsinki

HELSINKI 2014

ISBN 978-951-51-0388-8 (paperback)
ISBN 978-951-51-0389-5 (PDF)
Unigrafia Oy
HELSINKI 2014

Acknowledgments

First of all, I thank my supervisor Professor Samuli Siltanen (University of Helsinki) for his significant contribution, advice and guidance in this process. Without his encouragement and weird sense of humor this work would never be completed. The reviewers of this thesis, Dr Ozan Öktem (KTH Royal Institute of Technology, Stockholm) and Dr Aku Seppänen (University of Eastern Finland, Kuopio), deserve sincere thanks for their careful reading of the manuscript and detailed feedback.

I also wish to specially thank Dr Richard Webber, who revealed the secrets of limited angle tomography to me in numerous enthusiastic discussions in Winston-Salem and started this most demanding and rewarding process 18 years ago. This thesis has been written during the years 2009-2014 in several locations around the world. I want to thank all the fellows who have inspired me in the eye-opening discussions and presentations. Especially, I want to express my gratitude to my colleagues in Inverse Problems Society and my co-workers in Palodex Group.

I thank the Instrumentarium Foundation, the Academy of Finland and the Finnish Center of Excellence in Inverse Problems Research for financial support as well as the Palodex Group to give me this opportunity to work in this subject. This work have been done by using open source software, therefore I thank also those who are working in open-source projects. Especially the software teams in the Linux Foundation and the Free Software Foundation.

Mostly, I want to thank my Family, including the dogs, for their unconditional love, support and patience.

This thesis consists of an introduction and following four articles:

[I] A. Cederlund, M. Kalke and U. Welander, *Volumetric tomography - a new tomographic technique for panoramic units* **Dentomaxillofacial Radiology** (2009) 38, pp. 104–111

[II] M. Kalke and S. Siltanen, *Adaptive frequency-domain regularization for sparse-data tomography*, **Inverse Problems in Science and Engineering** (2013) vol 21, no 7 pp. 1099–1124

[III] M. Kalke and S. Siltanen, *Sinogram interpolation method for sparse-angle tomography*, **Applied Mathematics** (2014) vol 5, no 3 pp. 423–411

[IV] M. Kalke,*Method for the projection angle estimation in the x-ray tomography* (submitted)

The author had a major role in writing the articles [II], [III], [IV] and a co-author role in the joint article [I]. The author has done all numerical implementations and analysis in the articles [II], [III] and [IV] as well as the commercial implementation of the reconstruction method introduced in the article [I]. The author is the inventor of the methods described in the articles [II], [III] and [IV] and inventor in the reconstruction method described in the article [I]. The author is exclusive inventor of patents US7853056 and EP1793347, which are concerning the reconstruction method described in the article [I].

Contents

Acknowledgments 3
List of abbreviations 6
Abstract 7
1. Introduction 9
1.1. History of computed tomography imaging 10
1.2. Clinical benefits of tomographic imaging 11
1.3. Computed tomography apparatus 12
2. Reconstruction methods 15
2.1. Essential concepts for the reconstruction calculation 16
2.2. Filtered back-projection 19
2.3. Algebraic reconstruction technique 22
2.4. Regularized reconstruction techniques 24
3. Summary of the articles 26
3.1. Volumetric tomography 26
3.2. The WIRT method 30
3.3. The SINT method 32
3.4. The MINT method 35
4. Conclusion 37
5. Errata 38
References 39

List of abbreviations

1D	One dimensional
2D	Two dimensional
3D	Three dimensional
ART	Algebraic reconstruction technique
CBCT	Cone beam computed tomography
CT	Computed tomography
ENT	Ear, nose and throat
FBP	Filtered back-projection
FDK	Feldkamp-Davis-Kress (algorithm)
FOV	Field of view
GPGPU	General-purpose computing on graphics processing units
GPU	Graphics processing unit
kVp	Peak kilo volts
MAP	Maximum a Posterior
MART	Multiplicative algebraic reconstruction technique
MINT	Mutual Information based Technology
PSF	Point spread function
SART	Simultaneous algebraic reconstruction technique
SINT	Sinogram interpolation technique
SIRT	Simultaneous iterative reconstruction method
SVD	Singular value decomposition
TV	Total variation
VT	Volumetric Tomography
WIRT	Wiener-filter based Iterative Reconstruction Technique

Abstract

The purpose of medical computed tomography (CT) is to generate a three dimensional (3D) model of inner organs based on number of two dimensional (2D) X-ray images taken from different directions around the patient. Clinical CT imaging improves and extends the operational and diagnostic X-ray imaging since it basically adds a new spatial dimension to the data by converting multiple 2D images into a single 3D volume. From the volume representation it is possible to measure distances or observe relations between inner structures in detail.

The process that generates the 3D volume from number of projection images is generally called reconstruction process, which can be considered to consists of three stages: Pre-processing that modifies the projection images into suitable form for the reconstruction, reconstruction itself that generates a 3D model from the projection images and post-processing, which attenuates noise and other un-idealities and emphasizes the clinically relevant information. Each of these steps has an impact to the image quality and therefore has to be optimized to gain optimal image quality for the given clinical task.

Conventional CT design is not optimal in the sense of cost, workflow or dose for two reasons. Firstly, CT devices are typically expensive and bulky devices because they require a stable X-ray production, rigid gantry with accurate and repeatable movements, high scanning speed, solid patient support and a low-noise X-ray detector. Secondly, current non-regularized reconstruction techniques require high dose per projection image as well as a huge number of projection image. This also limits the usage of the CT imaging to serious trauma cases and other lethal diseases.

To overcome the limitations mentioned above, new approaches have been introduced. For example, year 2007 a dental imaging technology company Palodex Group (Tuusula, Finland) released an upgrade kit for standard digital panoramic X-ray device, named *Volumetric Tomography* (VT), which enables limited angle low dose 3D imaging for implant planning. VT can be considered as a limited angle tomography device since it acquires between 5 to 11 projection images from $40-45$ degree aperture with maximum 80 kVp X-ray energy, while in conventional dental CT device over 300 projection images are taken from $180-360$ degree aperture with $90-120$ kVp X-ray energy.

The limited angle tomography is a well-known example of ill-posed problem since the volume cannot be uniquely determined based on the projection image. It has been estimated in this study that typically only 10% of the information is defined by the projection data in extremely sparse and limited angle tomography. Therefore, novel image processing methods for pre-processing, post-processing and reconstruction are needed for feasible reconstruction quality from a limited number of projection images.

The purpose of this thesis was to evaluate the capability of the VT device for clinical implant planning and improve the reconstruction quality as well as the versatility of the VT concept. For that reason, novel imaging processing and analyzing methods were generated. These methods can also be adapted to other sparse or limited angle tomography related reconstruction methods.

In the article [I], we evaluated if VT -device can be clinically used for implant planning. Based on these encouraging results, the VT system was also commercialized. During the development phase three separate patents were filed and later accepted.

In the article [II], a new image processing method based on modification of the constrained least-square filter for extremely sparse situations was introduced. In this method, called *Wiener-filter based iterative reconstruction technique* (WIRT), we considered the uncertainty of the interpolation as noise and utilized the regularization only in the regions where the uncertainty is the dominating factor. This was possible by modeling the reconstruction process in the frequency domain, where the known frequency components are located on the lines defined by the well-known Fourier slice theorem.

In the article [III], a new sinogram estimation algorithm called *sinogram interpolation technique* (SINT) was created, where the missing sinogram columns were estimated based on the known sinogram columns. Since the underlying sine waves from the sinogram cannot be directly determined, a new concept called *warp* was defined, which can be considered as a local sum of the underlying sine waves. The numerical implementation clearly indicates that this method is more accurate and reliable than basic interpolation methods if the angular difference between the projection images is spacious.

In the article [IV], a method named *mutual information based technology* (MINT) was developed to estimate the imaging geometry directly from the projection data. Imaging geometry can be consider as information about a location of the X-ray source and detector at the moment when each projection image was taken. This information is essential for the reconstruction quality where even smallest error in the image geometry model causes artifacts. In this method, the imaging angles can be estimated based on the projection images without any external markers or additional constructions to the device. It was also indicated that the MINT method can be expanded to several other tomographic situations, including local tomography, fan- and cone beam tomography. These extensions were also implemented to the study that was executed with clinical data.

In addition to the methods mentioned above, we also demonstrated that limited angle tomography is able to give similar clinical information as full-scan CT devices in dental implant planning. Therefore, the implant planning could be executed more cost and dose effectively when suitable algorithms are applied throughout the reconstruction process.

1. Introduction

Nowadays, three dimensional (3D) X-ray images are needed for a wide range of clinical procedures. The 3D data is generated by a computed tomography (CT) device, which is a dedicated X-ray system that takes hundreds of projection images around the target and calculates a 3D distribution of the attenuation coefficient, *volume*, from those images. The method that calculates the volume from the projection images is called *reconstruction*. In addition to the projection images, the reconstruction also requires *imaging geometry*, which can be considered as spatial information of the X-ray source and detector for each individual exposure.

Although CT imaging has some benefits over two dimensional (2D) imaging, there are some drawbacks as well. The biggest concerns in CT imaging are the high device cost and the patient dose. However, it has been demonstrated that these weaknesses could be solved by implementing sparse or limited angle tomography methods.*Sparse angle tomography* means that the number of projection images is limited, while *limited angle tomography* specifies that the aperture of the scan is limited. There are no exactly determined or fixed limits for sparse or limited angle tomography conditions, but it is generally supposed that if these limitations have a significant impact to reconstruction quality, the terms sparse and limited angle tomography are applicable.

In this thesis, we consider both sparse and limited angle tomography situations. In the sparse angle tomography cases we used only $10 - 20$ projection images with about 180 scanning aperture, while in limited angle tomography same number of projection images are limited into 45 degrees aperture. The fundamental challenge in sparse and limited angle tomography reconstruction can be seen in Figure 1, which indicates that while in the full scan tomography (by its definition) all frequency components of the volume can be defined, typically only under 10% of the frequency components of the volume in limited or sparse angle tomography scan are known. This lack of information calls for novel image processing methods to achieve clinically acceptable image quality. See also figure 5f-h as an example how conventional reconstruction fails in limited and sparse tomography situations.

The high cost and extensive construction of a CT device is mainly caused by strict accuracy requirements for the gantry movements needed for modeling the geometry information. This inconvenience could be avoided by determining the imaging geometry either directly from projection images or from a set of fiducial markers. Still, the drawback of this approach is that it requires more sophisticated methods to determine the realized gantry movement.

Currently there is promising development on limited and sparse angle reconstruction methods. However, most of these studies have been concentrated only to the part on the reconstruction that converts the projection images into a 3D model and not considering the complete process form the detector data to the final volume.

For improved reconstruction quality additional image processing is also needed before and after the reconstruction. Therefore, we consider in this thesis the complete *reconstruction imaging pipeline*, which consists of three sub-processes; pre-processing, reconstruction and post-processing. The purpose of the pre-processing is to distinguish the un-idealities such as the detector read-out noise or corrupted detector readings from the projection images and generate linearized grayvalues

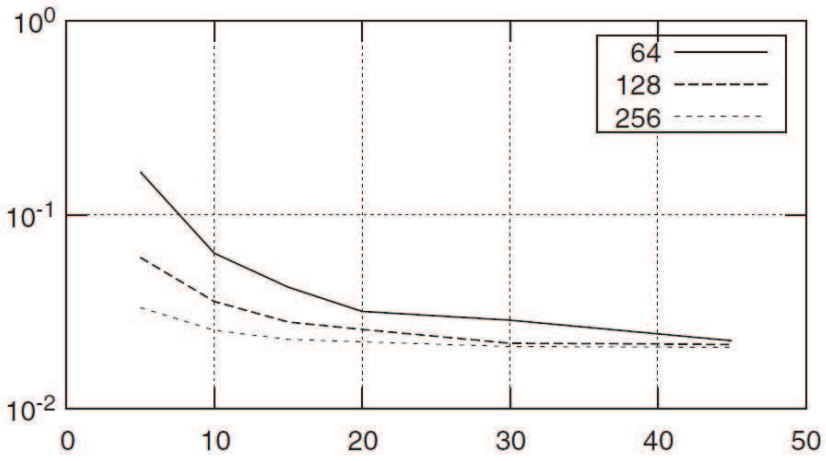

FIGURE 1. The fraction of known frequency components shown as function of sparsity (i.e. the angular difference between two adjacent projection images) for three different volume resolutions (64×64, 128×128 and 256×256). When sparsity increases above 10 degrees, less than 10% of information is defined by the projection data (see also Section 2.4). Originally published in the article [II].

for the reconstruction. Furthermore, after the reconstruction the clinically relevant information is emphasized in the post-processing stage. See [1, Section 2.3].

Before giving an overview about these new methods, we will discuss about historical, technical and clinical aspects of 3D imaging and explain some fundamental issues about 3D imaging and reconstruction calculation.

1.1. **History of computed tomography imaging.** The X-rays were discovered by German physicist Wilhelm Conrad Röntgen in the end of 19th century. The first official document about this significant discovery was a letter from Röntgen to the Physical Medical Society of Würzburg, dated December 1895. The X-ray source that Röntgen was using in his experiments was a Hittorf-Crookes -tube, which was very similar to the modern X-ray tubes. [2]

In the X-ray tube electrons are accelerated from anode to cathode by high voltage electrical field. When the electrons hit the cathode, their kinetic energy is partly transformed into electromagnetic radiation, which is capable to penetrate into the human body and partly attenuate there. The amount of the attenuation depends on the initial X-ray energy spectrum and the characteristics of the material. The sum of the attenuation can then be detected by screen, by film or nowadays mainly by digital detectors. [2]

The fundamental limitation of the X-ray image is that it indicates only the total sum of the attenuation from the X-ray source to the detector element instead of the exact position of the X-ray attenuation. To overcome this problem, A. E. M. Bocage invented 1921 the first *tomography* system, which was based on the synchronized

linear movement of the X-ray source and detector during the exposure. Since the X-ray source and the detector moved linearly to the opposite direction with a specific velocity, the projection of the object that lay in a fixed plane, called *focus plane*, was relatively stationary leading to a sharp image of objects in the focus plane, while all objects that are were located above or below were blurred out. See [1, Section 1.1].

Although Bocage's invention solves the initial problem of superposition, it has some disadvantages: Firstly, the focus plane has to be accurately defined before the X-ray scan. Secondly, there can be only one focal plane per scan. Thirdly, amount of blurring is weak near the focal plane leaving artifacts, called *off-focal shadows*, to the tomographic image. Despite these limitations, this tomography technique is still widely used for example in modern digital dental imaging devices [3–5].

The reconstruction calculation is based on the studies by Austrian mathematician Johann Radon, who showed in 1917 that 2D object can be reconstructed uniquely from infinite number of one dimensional (1D) projections. The transform from the object to the projection is called the *Radon transform*. The fundamental theory of the Radon transform and especially the inverse Radon transform, i.e. transformation from the projection images back to the object, are the basis of the numerical computed tomography. Before the inverse Radon transform was used in X-ray tomography, it was successfully applied in several other technologies from microwave emission of the sun to the television technology. [1, Section 1.2]

The first public documentation related to CT imaging was a patent granted as early as 1940 to Gabriel Frank. In this patent Frank clearly described the principle of CT imaging. Since during that time it was impossible to actually compute the slices because of limitations of digital imaging devices and computers, the outcome from the device described in this patent was a sinogram instead of slice or volume data. Therefore, there were hardly any interest on this innovation that time. [6, Section 2.3]

Another important milestone in the history of CT imaging was William H. Oldendorf's experiment in 1961, where he demonstrated that the internal structure of an object could be measured by utilizing an X-ray source, a photon multiplier and a gantry with a rotating and linear scanning movement. [1, Section 1.2]

In 1963 and 1964 Allan M. Cormack published results from a similar experiment as Oldendorf did several years earlier. However, unlike Oldendorf, Cormack also implemented a working reconstruction algorithm and was therefore able to reconstruct the internal structure of the object based on these measurements. For that reason, Cormack's experiment can be considered as a first functional CT system ever. [1, Section 1.2]

Independently from the Cormack's research work, Godfrey N. Hounsfield studied the tomographic problem in Central Research Laboratories of EMI Ltd in England. Based on the these studies, the development of the first clinical CT scanner started year 1967. Twelve years later Cormack and Hounsfield shared a Nobel price of Physiology and Medicine for their fundamental contribution in the CT imaging development. [1, Section 1.2]

1.2. **Clinical benefits of tomographic imaging.** Nowadays, there are multiple clinical applications based on CT imaging. One example is dental implant planning, where a missing tooth is replaced by an artificial one. In the implant planning application the optimal angle, depth and diameter of a screw hole have to be accurately

X-ray technique	Typical effective dose (μSv)
Intraoral	5
Cephalometric	6
Panoramic	19
Dental CT	200
Mammogram	400
Head CT	2 000
Chest CT	7 000
Lower gastrointestinal X-ray series	8 000
Coronary CT angiogram	12 000

TABLE 1. The effective dose of dental and medical X-ray techniques. Despite dental CT study has typically lower dose than medical CT examinations, it still gives significantly higher patient dose than other dental X-ray techniques [10–12]

.

defined: If the hole is too deep, the surrounding tissue is unnecessarily harmed. On the other hand, if the hole is too shallow, the attachment can be loose [7].

Another benefit of CT imaging is resolving the superposition problem. Superposition means that multiple inner structures overlap, causing a situation where the clinically relevant information is disturbed by extreme attenuation and photon starvation. This is a significant problem especially in low contrast imaging, like mammography. However, since in the 3D imaging multiple images are taken from different angles and the focal slice can be freely chosen, the clinical relevant information can be unveiled. [8] [9]

The biggest concern in CT imaging has always been the patient dose. Since CT imaging needs several projection images, the patient dose is significantly higher than in conventional X-ray study. For that reason, some CT imaging procedures are limited only to operations or diagnostic tasks where the high dose is justified, such as lethal disease treatments (see Table 1).

Lately there has been increasing interest on low-dose CT imaging, which could reduce the patient dose and expand the 3D imaging into less severe diseases or cosmetic operations. The dose reduction is gained by decreasing the number of the projection images, total scanning aperture and tube energy. However, this approach requires also specific reconstruction algorithms to accomplish the clinical task. In several clinical studies, significant dose savings have been reported by implementing more advanced computing methods. [13–18]

1.3. **Computed tomography apparatus.** Digital X-ray images are projection images, where each picture element, *pixel*, value is proportional to the amount of X-ray flux that falls to the pixel area. If the initial X-ray flux is known, the sum of the attenuation along the X-path can be defined based on the single image [1].

[1]To be exact, there are also other phenomenons, for example beam hardening and scattering, that are ignored in current reconstruction algorithms and compensated later in post-processing. For more detailed information, see for example [2, Section 3] and about the compensation refer [1, Section 7]

To generate 3D volume, the exact location of the attenuation has to be known, which requires several projection images around the object and the corresponding imaging geometry information. See [19, Section 3].

For example, in a dental CT system, typically hundreds of images are taken around the object [16–18]. The exposure pulses during the scan are relative short and therefore each projection image is considered as a stationary image. During the calibration process, the location of the X-ray source and the detector are recorded for each projection. After the calibration process has been completed, the scanning movement is assumed to be repeatable. Typically, but not necessarily, the X-ray source and the detector are rigidly mounted to one block, called *gantry*, that rotates around the object. In such a case, if the mechanical dimensions of the device are known, the imaging geometry is solely defined by the gantry angle, called *projection angle*.

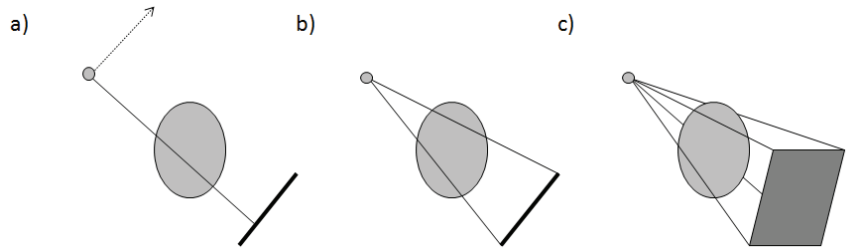

FIGURE 2. Classification of projection image geometries. a) Parallel-beam imaging geometry with a linear scanning movement. The X-ray beams are orthogonal throughout the detector. b) Fan-beam imaging geometry where the X-ray beams diverse in one dimension form the stationary source. c) Cone-beam imaging geometry where the X-ray beams diverse in two dimensions.

1.3.1. *Imaging geometry of the projection image.* The imaging geometry plays an important role in the reconstruction calculation. The imaging geometry of a single projection image can be either *parallel-beam*, *fan-beam* or *cone-beam* depending on the scanning movement and the detector type. In parallel beam geometry, all X-ray beams are parallel to the detector plane while in fan-beam geometry the X-rays deviate from the source causing a fan-shape flux. Furthermore, in cone beam imaging geometry the deviation exists in both horizontal and vertical directions (see Figure 2). The aperture of a single projection image in fan- and cone-beam geometry is called the *fan angle*. See [20, Sections 3.4 and 3.5] and [21, Section 5.11.6].

Parallel beam imaging geometry is not a practical solution for modern CT scanners, because it requires an additional linear scanning movement for each independent projection image, which leads to more complex mechanical structure and longer scanning times. However, parallel beam imaging geometry is widely discussed in many theoretical studies and articles since it simplifies the reconstruction

calculation. Moreover, since other imaging geometries can be converted into parallel beam situation by implementing an additional re-sampling step, the methods that are introduced in the parallel beam situations can also be inevitably applied into other imaging geometries as well. [1, Section 3.5.3].

Because of the decreasing price of large area X-ray sensors and request for faster scanning times, the fan- and cone beam systems have replaced parallel beam systems in the CT imaging. There are two detector types for fan- and cone beam devices; equi-spaced and equi-angular detectors. An equi-angular detector consists of multiple detector modules that are concentric to the X-ray source, while the equi-spaced approach is used in the single-module detectors, such as flat-panels or detector with image intensifiers. CT devices that utilize flat single-module detectors are generally called *cone beam computed tomography* (CBCT) devices. As an example, see Figure 3. [1, Section 3.5]

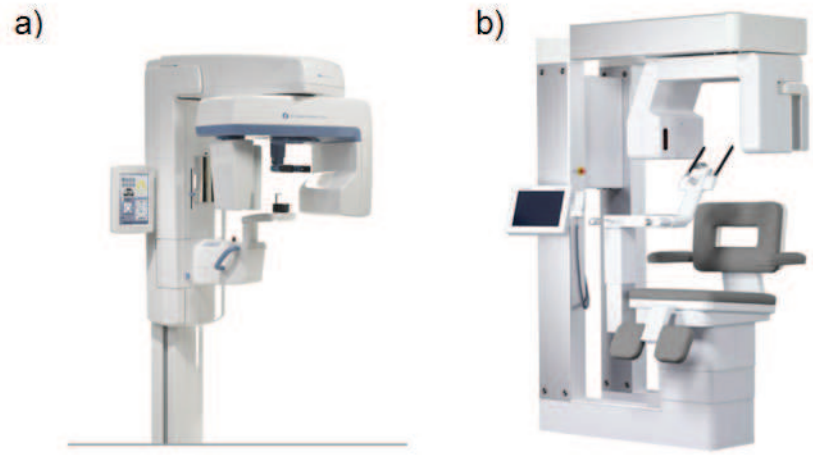

FIGURE 3. Examples of CBCT devices for dental imaging purpose. a) Orthopantomograph® OP300 device (manufactured by Instrumentarium Dental, Tuusula, Finland) for 3D, panoramic and cephalostatic imaging. b) SCANORA® 3D device (manufactured by SOREDEX, Tuusula, Finland) for 3D and panoramic imaging. Original image courtesy of Palodex Group (Tuusula, Finland).

1.3.2. *Imaging geometry of the tomography scan.* Computed tomographic scans can be divided into three categories based on the aperture of the scan: *Full scan*, *limited scan* and *sparse scan*. In a full scan, the number of projection images and aperture of the scan are sufficient to gain a uniform and isotropic resolution in the volume [2] (see Figures 4a and 5b). In practice, a full scan requires 180 degrees aperture when parallel beam geometry is used and over 360 degrees aperture when fan- or

[2]In this thesis, we apply term uniform to indicate that the resolution does not spatially vary and isotropic to indicate that the resolution is independent from the viewing angle in the volume

cone-beam geometry is applied. Secondly, sparse scan means that the number of projection images is insufficient to gain isotropic resolution, but the aperture of the scan is unlimited (see Figures 4c and 5c). Thirdly, limited angle scan means that the scanning aperture is strongly limited (see Figures 4b and 5d). In some literature, limited angle tomography reconstruction techniques are called tomosynthesis. [13]

Since in sparse and limited angle scans the artifacts limit the suitable viewing angle of the reconstructed volume, the projection angles of the scan have to be chosen beforehand based on the given clinical tasks. Typically only when viewing the volume from similar angle as projection images were taken, the quality is suitable. From other viewing directions, the result is not blurred or disturbed by artifacts. Theory behind this phenomenon will be later discussed in the Section 2.1.2.

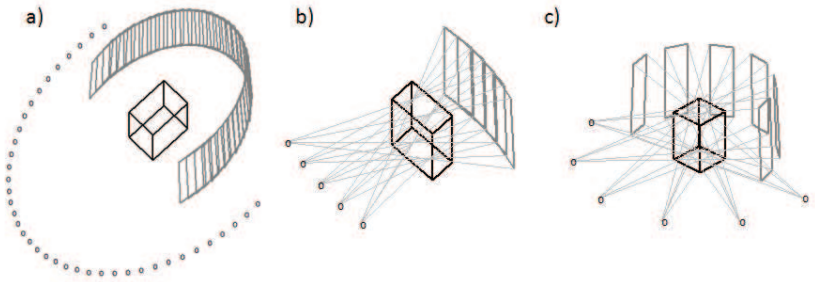

FIGURE 4. Classification of scanning apertures. a) Full angle scan with 195 projections, b) limited angle scan and c) sparse scan with 5 projections. In the Figure a) every fifth projection is plotted and all cone lines are removed for clarity.

2. Reconstruction methods

As already mentioned in the Section 1, the purpose of the reconstruction algorithm is to generate a 3D volume that spatially models the X-ray attenuation inside the target object. As an input data, the reconstruction requires *tomographic data*, which consists of the projection images and related imaging geometry information to generate a 3D volume as an output data.

The reconstruction algorithm can be either non-iterative, e.g. *filtered backprojection* (FBP), or iterative, e.g. *algebraic reconstruction technique* (ART). The benefits of iterative reconstruction include more accurate modeling of various tomographic imaging situations and better handling of ill-posedness arising for example from limited tomography or noisy projection data. These benefits are based on more advanced and versatile modeling of the imaging, not the iterative nature itself. However, typically non-iterative reconstruction offers similar image quality in significant shorter time when the number of images and scanning aperture are sufficient. See [1, Section 3.6.1] and [20, Section 7].

The drawback of ART and FBP reconstructions is that they do not include any regularization. In regularized reconstruction methods a priori information of the object is implemented into reconstruction process to improve the stability. In practice, this is handled by adding an additional cost function to the reconstruction

algorithm that it complements the ill-posed problem into a well-posed problem. This addition typically improves the convergence rate as well.

The result of the reconstruction consists of volume elements, *voxels*, which can be considered as smallest addressable and controllable units in the volume. Inside the voxel the attenuation is modeled as a constant number and defined typically in Hounsfield scale, where zero is equivalent to the attenuation of water and -1000 is equivalent to the attenuation of air. See [19, Chapter 3].

In the next Sections 2.2-2.4 we will introduce three common reconstruction techniques; FBP, ART and regularized reconstruction. Before introducing these reconstruction algorithms in detail, two essential mathematical methods related to the reconstruction algorithms are introduced. The first method is the Radon transform, which offers a mathematical model for the X-ray projection. The second method is the Fourier slice theorem, also known as the projection theorem or central slice theorem, which has several implementations in reconstruction calculation. We also introduce a concept called *sinogram*, which is a specific representation of a discrete projection data. For the sake of simplicity, we have considered the volume as a 2D object and the detector as an 1D object, unless otherwise mentioned. See [22, Chapter 10.4] and [21, Section 5.11.4].

2.1. **Essential concepts for the reconstruction calculation.**

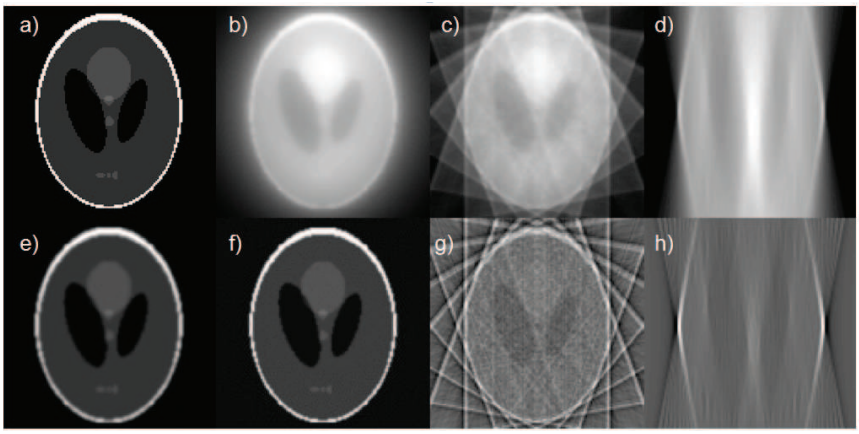

FIGURE 5. Reconstructions from the Shepp-Logan phantom. a) Shepp-Logan phantom. b) Full scan back-projection from 180 projection images, aperture of 180 degrees. c) Sparse angle reconstruction from 9 projection images with a same aperture. d) Limited angle reconstruction from 9 projection images with aperture of 20 degrees. e) Full scan FBP with Ram-Lak and Hanning filter. f) Full scan FBP reconstruction g) sparse angle FBP reconstruction and h) limited angle FBP reconstruction. In the Figures f) to g) Ram-Lak filter was applied and projection angles were same than in the Figures b) to d).

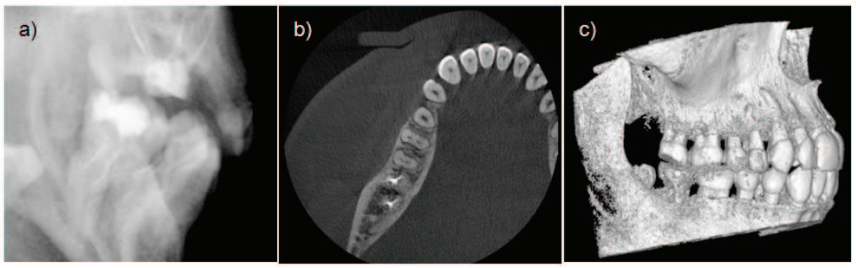

FIGURE 6. In the 3D viewing applications, the volume is typically represented either as individual slices or as a rendered 3D volume, which is basically generated by stacking the slices. Example of images related to CT scan a) one of the projection images, b) a single reconstructed axial slice and c) a rendered 3D volume from the same region.

2.1.1. *Radon transform.* A parallel X-ray projection of an object $f(x, y)$ can be modeled as a sum of attenuation values across the X-ray beam as

$$g_k(t) = \int_{-\infty}^{\infty} \int_{-\infty}^{\infty} f(x, y)\delta(c(t, \theta_k))dxdy, \tag{1}$$

where $k = 1, 2, 3 \ldots K$ is the projection number, $t \in \mathbb{R}$ is the projection point in the line perpendicular to the X-ray beam and the function $c(t, \theta_k) = x \cos\theta_k + y \sin\theta_k - t$ is normal representation of a line that has angle of θ_k with respect to the x-axis and distance t from the origin. Furthermore, the function δ is the unit impulse, i.e:

$$\delta(c) = \begin{cases} 1 & \text{for } c = 0 \\ 0 & \text{otherwise.} \end{cases} \tag{2}$$

The equation (1) is called (forward) Radon transform. It defines the transformation from the 2D object $f(x, y)$ to the 1D projection $g_k(t)$.

2.1.2. *Fourier slice theorem.* The Fourier Slice theorem defines the frequency components that are defined by the projection images and their angles. The Fourier slice theorem states that (as written in [1, Section 3.3]):

> The Fourier transform of a parallel projection of an object $f(x, y)$ obtained at known angle θ equals a line in a 2D Fourier transform of $f(x, y)$ taken at the angle θ.

In mathematical terms we can describe this as

$$G(\omega, \theta_k) = F(u, v) \quad \text{,where} \quad \begin{cases} u = \omega \cos\theta_k \\ v = \omega \sin\theta_k \end{cases} \tag{3}$$

In the equation (3) ω is frequency component and θ_k is the corresponding projection angle (see Figure 7). Moreover, $G(\omega, \theta_k)$ is a 1D Fourier transform of the projection $g_k(n)$ defined as

$$G(\omega, \theta_k) = \mathcal{F}(g_k(t)) = \int_{-\infty}^{\infty} g_k(t)e^{-j2\pi\omega}dt \tag{4}$$

and similarly $F(u,v)$ is 2D Fourier transform of $f(x,y)$

$$F(u,v) = \mathcal{F}(f(x,y)) = \int_{-\infty}^{\infty}\int_{-\infty}^{\infty} f(x,y)e^{-j2\pi(ux+vy)}dxdy. \tag{5}$$

The Fourier slice theorem has several important consequences. Firstly, this theorem defines the upper limit for the spatial reconstruction resolution when the number of projection images, pixel size and angles are known. Secondly, it improves the back-projection operation computing time; instead of copying all pixel values back to the volume, the Fourier transform of each projection image can be copied into the single line in frequency domain and then perform 2D inverse Fourier transform to gain the final reconstruction. Thirdly, the Fourier slice theorem offers a theoretical framework for the filtering in FBP reconstruction.

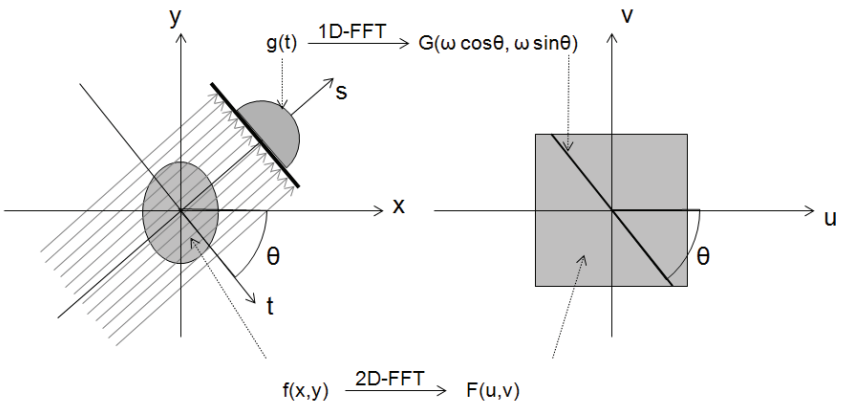

FIGURE 7. Fourier slice theorem defines the relation between the spatial (left) and the frequency domain (right) in tomography. A single parallel beam projection image taken with θ degree projection angle defines frequency components in a single line with angle θ respect to the horizontal frequency axis.

2.1.3. *Sinogram.* In the previous chapter, we considered the projection as a continuous data. However, in practice the readings of digital detectors are discrete data. To create a discrete representation of the projection $g_k(t)$, we introduce a matrix $S \in \mathbb{R}_+^{N\times K}$, which consists of sampled detector readings from a tomography scan such that each value $S_{n,k}$ is a grayvalue of a single detector pixel, where $n = 1,2,3\ldots N$ is the pixel index and k is the projection index (as before) related to the value t such that

$$S_{k,n} = g_k(t) \quad \text{,such that} \quad n = \left[(N-1)\frac{t-t_{\min}}{t_{\max}-t_{\min}}\right] + 1, \tag{6}$$

where $[\cdot]$ is rounding operator to nearest integer and $t_{\min,\max}$ are the minimum and maximum values for t. The matrix S is commonly known as *sinogram*, where each column is a projection image in ascending projection angle order such that $\theta_1 < \theta_2 < \theta_3 < \ldots \theta_{K-1} < \theta_K$. In sinogram representation, each point in the object

$f(x, y)$ generates a sine shaped wave where the amplitude is proportional to the distance between the point and the rotation axis (see Figure 8b as an example). See [21, Section 5.11.3].

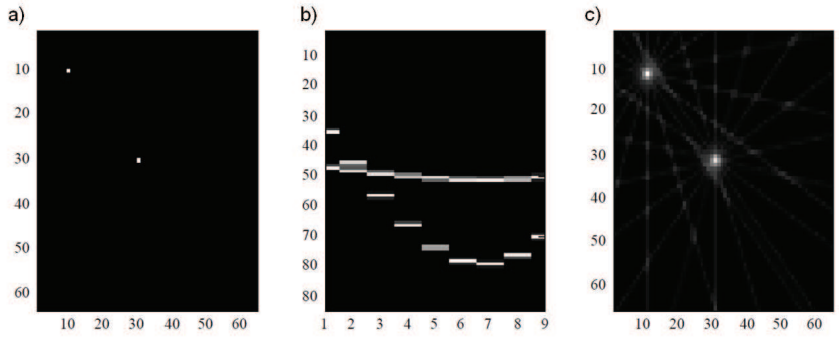

FIGURE 8. Example of sinogram representation. a) The original object with two non-zero points. b) The sinogram presentation of the same object when nine images are taken from 20 to 180 degree angles. c) The reconstruction done from the projection data by using back-projection algorithm. Originally published in the article [III].

2.2. **Filtered back-projection.**

2.2.1. *Back-projection algorithm.* The Radon transform described in the equation (1) determines the projection g when the object f is fixed. However, in X-ray tomography our intent is to define the object based on noisy projection images, which is therefore considered as inverse problem [3]. This is achieved by the back-projection operator $\mathcal{B}(\cdot)$, where each element of the g is copied back to the volume across the line $c(t, \theta_k)$, which is in practice the direction of the X-ray beam. The reconstruction $\hat{f}(s, t)$ is then the normed sum over all back-projections

$$\hat{f}(s,t) = \mathcal{B}(g) = \frac{1}{K}\sum_{k=1}^{K} g_k(t) \quad \text{where} \quad \begin{cases} t = x\cos\theta_k + y\sin\theta_k \\ s = -x\sin\theta_k + y\cos\theta_k \end{cases} \tag{7}$$

for all s.

Although in theory $\lim_{K\to\infty} \hat{f} = f$ holds, it should be fully understood that $\hat{f}$ is only a approximation of the original object f when K is a finite number or any kind of un-idealities or noise in tomographic data is present. This can be demonstrated by considering a simple object where $f(x_i, y_j) = 1$ and zero elsewhere. Then, based on equation (1), each projection image g_k has also a single value of one and zero elsewhere. However, the back-projection operation $\mathcal{B}(g)$ in equation (7) generates K lines across the volume $\hat{f}(x, y)$ that intersects at the point (x_i, y_j). With small

[3] To be exact, the justification of concerning the tomography as an inverse problem is based on the fact that, unlike the projection images, the attenuation in the volume cannot be directly measured. [23, Chapter 1]

value of K, the reconstruction is heavily distorted by individual lines. When the value K increases, the number of these lines increases and finally they generate a blurred point. Despite the fact that reconstruction quality improves when the number of projections K increases, perfect reconstruction is never achieved with a finite number of projections even in noiseless situation.

2.2.2. *Filter design.* The blurring effect of the back-projection operation described above can be observed also in the Figure 5b. To compensate this blurring, a high-pass filter is applied. The theory of the filter design is based on Fourier slice theorem as introduced in the section 2.1.2.

The 2D inverse Fourier transform for the object is

$$f(x,y) = \int_{-\infty}^{\infty}\int_{-\infty}^{\infty} F(u,v)e^{j2\pi(ux+vy)}dudv. \tag{8}$$

Since $u = \omega\cos\theta$ and $v = \omega\sin\theta$ we get from the Fourier slice theorem (equation (3)) that

$$dudv = \begin{pmatrix} \delta u/\delta\omega & \delta u/\delta\theta \\ \delta v/\delta\omega & \delta v/\delta\theta \end{pmatrix} d\omega d\theta = \omega d\omega d\theta, \tag{9}$$

then equation (8) transforms to form

$$f(x,y) = \int_{0}^{2\pi}\int_{-\infty}^{\infty} F(u,v)e^{j2\pi(ux+vy)}\omega d\omega d\theta. \tag{10}$$

In the parallel beam projection, two projections π apart have exactly the same set of ray path in reverse order such that $g(t,\theta) = g(-t,\pi-\theta)$ and therefore also $G(\omega,\theta) = G(-\omega,\pi-\theta)$. Then, from the equations (3) and (10) we see that

$$\hat{f}(x,y) = \int_{0}^{\pi}\int_{-\infty}^{\infty} |\omega|\, G(\omega,\theta)e^{j2\pi\omega t}d\omega d\theta, \tag{11}$$

where $t = x\cos\theta + y\sin\theta$.

In equation (11) the term $|\omega|$ is a ramp filter, called *Ram-Lak filter*, which attenuates the blurring effect of the inverse Radon transform (see Figures 5f-5h).

Still, there is a drawback in applying the Ram-Lak -filter. The high-pass nature of this filter is very sensitive to geometry inaccuracies as well as the noise in the detector reading as indicated in the Figures 5f-5g. This is compensated by multiplying the Ram-Lak filter by a low-pass filter, such as Hamming, Box or Hann -filter. This low-pass filter can also be designed such that it crops the frequencies above the Nyquist frequency and therefore works as an anti-aliasing filter. When the filter is added to the equation (11) we get

$$\hat{f}(x,y) = \int_{0}^{\pi}\int_{-\infty}^{\infty} |\omega|\, H(\omega)G_{\mathrm{zp}}(\omega,\theta)e^{j2\pi\omega t}d\omega d\theta, \tag{12}$$

where $\hat{f}(x,y)$ is the FBP reconstruction of the object $f(x,y)$, $H(\omega)$ is the filter combination mentioned above and G_{zp} is zero-padded Fourier transform of the projection image (see Figures 5e-5f). For further information about the filtering, zero-padding and sampling theory, see [21, Section 4.6]

In practice the FBP reconstruction is executed in multiple phases. The details of these steps are typically company confidential information based on clinical know-how and subjective image quality rather than strict mathematical theory.

Especially since each CT device design has its own characteristic noise and unidealities, device specific image processing and dedicated calibration routines are typically needed.

2.2.3. *FBP modifications for the fan- and cone-beam imaging geometries.* The discussion so far has been on parallel beam imaging geometry while the imaging geometry of the modern CT is based on fan- or cone beam imaging geometry (see discussion in the Section 1.3.1). Consequently, the results from the previous Sections 2.1.1-2.2.1 cannot be applied directly. However, the fan-beam geometry can be transformed into parallel beam geometry by using following conversion

$$\begin{aligned} \theta &= \beta + \gamma \\ t &= D \sin \gamma \end{aligned} \tag{13}$$

where D is the distance between the X-ray source and iso-center, β is the projection angle γ is called *detector angle*, which is the angular deviation of each x-ray path from detector normal normal (see Figure 9).

One approach to convert fan-beam geometry into parallel beam geometry is a *re-binning* method, where fan-beam projection images are first re-projected into iso-center plane. Then, additional weighting operation is applied before the actual filtered back-projection process. This can be effectively executed in the sinogram domain. See [1, Chapter 3.5.3] and [21, Section 5.11.6].

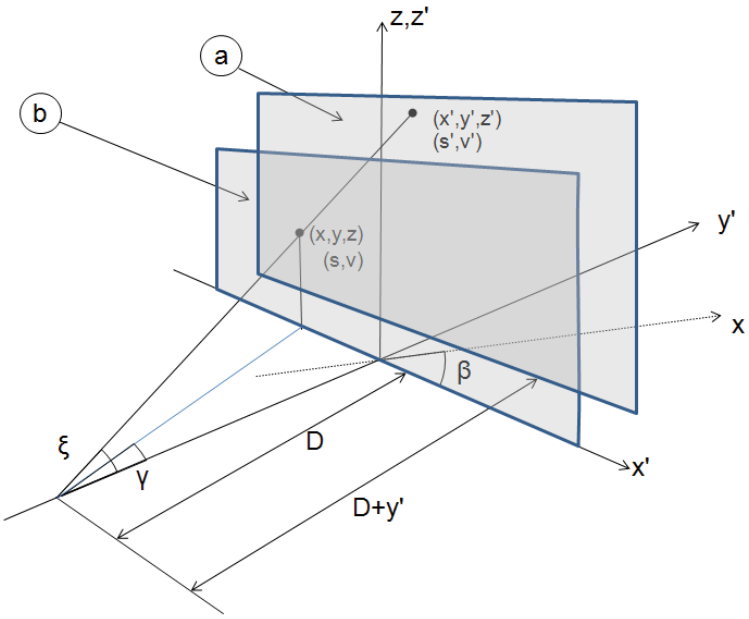

FIGURE 9. Parameters used in the FDK-algorithm (see equation 14). In the FDK method projection image (a) is remapped to the imaginary detector (b) that is considered as a single layer in the volume.

One of the most implemented reconstruction algorithm for CBCT devices with equi-spaced detector is Feldkamp-Davis-Kress (FDK) algorithm. The FDK algorithm is based on re-projection, where each projection image is re-projected to imaginary detector located in the iso-center with projection angle θ (see Figure 9). The re-projection is done directly in three dimensional domain by using weight factors that are defined similarly to the fan beam case. The FDK algorithm has several deviations, one intuitive approach is described in Hsieh book [1, Section 10.3] as

$$\hat{f}(x,y,z) = \frac{1}{2}\int_0^{2\pi}\left(\frac{D}{D+y'}\right)^2 d\beta \int_{-\infty}^{\infty}\cos(\xi)q(s,v,\beta)h(s'-s)ds. \tag{14}$$

where the parameters are defined in the Figure 9. Here the reprojected projection image q is filtered by the band-passed filter h and weighted based on the deviation from the iso-ray and on the magnification factor. As discussed in Section 2.2, the filter h includes Ram-Lak and low-pass filters as well as zero-padding operator.

The cone-beam imaging geometry has several theoretical challenges compared to the parallel-beam imaging geometry. The FDK algorithm gives sufficient reconstruction quality near the x-y plane, but when the distance form the x-y plane increases, also the sampling rate decreases. This generates artifacts to the top and bottom of the reconstruction when a circular trajectory is applied. To overcome this sampling problem, alternative trajectories with varying z-position of the focal spot are proposed. For an overview to the FDK algorithm refer to [1, Section 10.3], for the original article about the FDK method see [24].

2.3. **Algebraic reconstruction technique.** Despite the fact that FBP is the most implemented reconstruction method in commercial CT systems, there are some major imperfections in this method. Firstly, FBP method is based on the inverse Radon transform that models both the X-ray source and detector elements as non-dimensional points, which does not represent the real imaging situation. Secondly, inevitable noise is not explicitly modeled in the FBP algorithm. Thirdly, the FBP algorithm cannot handle ill-posed situations such as limited or sparse imaging geometries, because of the lack of the regularization. ([1] Section 3.6.1)

To correct the flaws mentioned above, new iterative reconstruction algorithms have been developed such as Prior Image Constrained Compressed Sensing (PICCS) or Ordered Subset Separable Paraboloid Surrogates (OS-SPS) [25–29]. Nowadays, the most studied and implemented iterative method is the ART reconstruction, where both measurement (i.e. all detector readings of the scan) $m \in \mathbb{R}_+^M$ and the voxel values of the volume $x \in \mathbb{R}_+^N$ are modeled as vectors in a multidimensional domain. Moreover, the imaging geometry is included in *geometry matrix* $A \in \mathbb{R}_+^{M\times N}$, where each matrix element a_{ij} indicates contribution of a voxel x_i attenuation to the detector reading m_j.

$$m = Ax + \varepsilon, \tag{15}$$

where ε is the additive measurement noise. The model described in the equation (15) allows more realistic and versatile approach to the tomographic problem than Radon transform based approaches such as FBP. [20, Chapter 7]

From the equation (15) the X-ray projection m can be determined when the imaging geometry A, volume x and noise ε are known, which is considered as the forward problem in the tomography. However, in the tomographic calculation, the

task is to determine the volume x when the imaging geometry matrix A and the projection image vector m are fixed, which is considered as the inverse problem. The vector x can be defined from the equation (15) directly only if A is invertible, well-conditioned and noise ε is known. None of these statements hold in a tomographic problem.

The strategy in ART algorithm is to find a volume $\hat{x}$ which minimizes the L_2 norm of the noise ε, which is therefore considered as residual between the projected volume and measurements. Then

$$\hat{x} = \underset{x}{\operatorname{argmin}} \, |Ax - m|_2^2, \tag{16}$$

which is achieved when

$$\hat{x} = \left(A^T A\right)^{-1} A^T m. \tag{17}$$

and $A^T A$ is non-singular. Solving equation (17) directly is impractical, since the size of the matrix A is extensive. For example, for a scan of 600 projection images each consisting 400×400 pixels and a volume of $256 \times 256 \times 256$ voxels, we get over $1.6 * 10^{15}$ elements for the matrix A. It is obvious that generating the matrix A or determining the inverse of the matrix $A^T A$ is computationally impractical.

For that reason, ART calculation utilizes a matrix free approach, based on *Kaczmarz's iteration* procedure, where each row in the matrix A is considered as a $N-1$ dimensional hyperplane. In this method, first an initial guess for the volume is created, say $x^{(0)}$, and projected to the first hyperplane defined by a linear equation $< a_1, x >= m_1$, where a_1 indicates the first row of the matrix A. The projection point in the hyperplane is then considered as the next estimate $x^{(1)}$ for the volume. This process is repeated until feasible estimate for the volume x is found or a criteria for residual ε is fulfilled. The estimate for the volume x on the iteration round r is then

$$x^{(r)} = x^{(r-1)} - \lambda \frac{\langle a_j, x^{(r-1)} \rangle - m_j}{< a_j, a_j >} a_j, \tag{18}$$

where λ is a relaxation factor, which is implemented to improve the convergence rate. It is known that $\lim_{r \to \infty} x^{(r)} = \hat{x}$ when $0 < \lambda < 2$. [30, Section 2.4.2].

There are many variations of ART algorithms, but essentially they all utilize Kaczmarz's iteration technique to minimize the residual described in equation (16).

One commonly referred variation of the ART method is simultaneous iterative reconstruction method (SIRT), where the current guess of the volume is updated after calculating the residual against all projection images. Then the iteration is then formulated as

$$x^{(r)} = x^{(r-1)} - \frac{\lambda}{\sum_{j=1}^{M} a_{ij}} \sum_{j=1}^{M} \frac{\langle a_j, x^{(r-1)} \rangle - m_j}{\sum_{i=1}^{N} a_{ij}} a_{ij}. \tag{19}$$

Since the number of updates is less than in equation (18), SIRT offers faster convergence rate and prefers more blurred estimate than basic ART but more blurred result. [20, Section 7.3] Another frequently referred variation of the ART is simultaneous algebraic reconstruction technique (SART), which is based on simultaneous correction of all rays in same projection. Moreover, a Hamming window and bi-linear interpolation are implemented in the back-projection stage to gain a smoother result for the reconstruction. The benefit of the SART approach is

more efficient convergence rate than in conventional ART reconstruction. Typically SART requires only one iteration round for sufficient reconstruction result. See [31] and [20, Section 7.4].

Third important deviation of the ART algorithm is multiplicative algebraic reconstruction technique (MART), where the residual is defined as a relation between back-projected current guess and corresponding measurement. the MART algorithm can be formulated as

$$x^{(r)} = x^{(r-1)} \left(\frac{m_j}{\langle a_j, x^{(r-1)} \rangle} \right)^{\lambda}. \tag{20}$$

MART offers better contrast than other ART methods, but it requires an exception handling for the case when $\langle a_j, x^{(r-1)} \rangle = 0$ and therefore it is less suitabel for parallel computing, like graphic processing unit (GPU) techniques.

For more discussion about ART algorithms and its variations, see for example [20, Section 7.5] and references within. Examples of ART reconstructions can be find from the article [II] Figures 4 and 5.

2.4. **Regularized reconstruction techniques.** Despite the fact that ART has been considered to be superior reconstruction technique compared to the FBP, because its more versatile geometry modeling and implicit noise modeling, it still lacks regularization, which is beneficial in limited and sparse angle tomography where the volume cannot be uniquely defined based on the projection images.

Regularization is based on *a priori information*, which is considered as additional information about the target object that is independent from the measured data (i.e. projection images). For example, if the type of attenuating material in the volume is known beforehand (e.g. volume typically includes air, bone, soft issue and teeth), one could prefer reconstruction solution that includes expected attenuation factors. Other examples are preferring smooth objects or sharp edges in the final reconstruction volume. This can be implemented to the reconstruction process by adding a cost-function with suitable norms.

Before the regularized reconstructions are explained in detail, we introduce two important concepts related to the regularization in the reconstruction; namely the *ill-posed situation* and the *Bayesian framework*.

The circumstances for the well-posed problem can be defined by the Hadamard's conditions, which are:

(1) A solution exists
(2) The solution is unique
(3) Behavior of the solution hardly changes when there's a slight change in the initial condition

If any of the conditions mentioned above is missing from the initial problem setting, the problem is called an ill-posed problem. Since at least the second Hadamard's condition does not apply in the limited or sparse angle tomography, they are considered as ill-posed situations by the nature. Moreover, if noise is dominating the result, also the third Hadamard's condition is lacking. [23]

In this thesis, the Bayesian framework has been chosen because it fluently combines the well-defined forward problem (projection) to the ill-posed inverse problem (back-projection) by implementing a priori information to the reconstruction. The

Bayesian interpretation of the tomography problem is

$$p(x|m) = \frac{p(m|x)p(x)}{p(m)}, \tag{21}$$

where x is the 3D volume and m is the measurements as before and $p(\cdot|\cdot)$ is the conditional probability. Moreover, $p(x|m)$ is called *posterior density*, $p(m|x)$ is the likelihood and the $p(x)$ is prior density. Since the term m is fixed during the optimization process, also the term $p(m)$ is constant and therefore it can be considered only as a scaling factor and later ignored. See [30, Section 3.1].

One computationally effective way to find a suitable estimate for x, say $\hat{x}$, is to find maximum point of the posterior probability $p(x|m)$ when a priori model and the measurement m are fixed, then the value $\hat{x} = \underset{x}{\operatorname{argmax}}\ p(x|m)$ is called *maximum a posteriori* (MAP) estimate. If both likelihood and priori probability density functions are considered as normal distributions, then

$$\hat{x} = \underset{x}{\operatorname{argmax}}\ p(x|m) \propto \underset{x}{\operatorname{argmin}}\ \left\{ |Ax - m|_2^2 + \alpha \left| Lx \right|_q^q \right\}, \tag{22}$$

where the first term $|Ax - m|_2^2$ is called likelihood term (see Section 2.3) and the term $|Lx|_q^q$ is called prior term, where $L \in \mathbb{R}^{N \times J}$ is typically a spatial differential operator. Furthermore, the term $\alpha > 0$ is called *regularization parameter* that balances the effect of the likelihood and the prior in the posterior density.

The most common regularization type in the literature is *Tikhonov regularization* mainly because of its simplicity and demonstrative nature. In the Tikhonov regularization the parameter $q = 2$ and L is the identity matrix. However, since Tikhonov regularization prefers smooth solutions for the volume, it is not the optimal prior in X-ray tomographic problems. [23, Chapter 5]

Currently, the most promising prior distribution in tomography is the total variation (TV), also in some articles called *lasso*, which minimizes the L_1 -norm of the local difference. The benefit of the L_1 norm is that, unlike Tikhonov regularization, it preserves sharp edges and regions with constant grayvalues in the reconstruction. In the TV approach the norm type is fixed as $q = 1$ and differential operator L is defined as

$$L_{ij} = \begin{cases} 1 & \text{if } i = j \\ -1 & \text{if } x_i \text{ and } x_j \text{ are adjacent voxels} \\ 0 & \text{otherwise} \end{cases} \tag{23}$$

The iterative reconstructions, e.g. ART or regulated reconstructions, require more computing time and resources than conventional FBP calculation. However, since the general-purpose computing on graphics processing units (GPGPU) -technology has become more cost-effective and the GPGPU coding is nowadays more practical, the iterative reconstructions have recently been implemented also to some commercial CT devices such as SCANORA® 3D CBCT device [4]. Moreover, recently also some major medical companies, for example GE Healthcare and Philips, have also implemented iterative reconstruction as an option to their medical CT devices. [15]

Finally, we want to point out that the regularization approach described above can also be achieved without introducing the Bayesian context. However, the

[4]SCANORA is registered trade mark by SOREDEX, Palodex Group, Tuusula, Finland

Bayesian approach is a simple and illuminating example how the tomographic inverse problem and the forward problem can be combined by implementing a priori information.

3. Summary of the articles

The purpose of this thesis was to evaluate the capability of the Volumetric Tomography (VT) for clinical implant planning and improve reconstruction quality as well as versatility of this concept. This thesis includes four scientific papers.

The article [I] clinically proves that limited angle tomography can be used in the implant planning with significantly reduced device cost and patient dose by combining a standard panoramic device, a novel reconstruction technique and usage of reference markers. Next two articles, [II] and [III], introduce innovative image processing methods that improve significantly the reconstruction quality in sparse and limited angle situations. The article [IV] describes a novel method for estimating the imaging angle based on the projection data without any external markers or other additional constructions. This significantly improves the workflow and versatility of the limited angle tomography.

In all these articles we consider limited or sparse angle tomography, similar to VT, where less than 20 images are taken. In this kind of situation, the part of the known frequency components is under 10% of all frequency components (see Figure 1) and therefore we considered it as a extremely ill-posed situation where the basic FBP reconstruction techniques do not provide sufficient image quality as indicated in the Figure 5.

In this Section 3 we introduce these methods, discuss about the results and future plans on limited and sparse angle tomography.

3.1. **Volumetric tomography.**

Currently there are several CBCT devices on the market, which are dedicated to the dental and head area imaging. These devices are mainly used for implant planning, where missing or damaged teeth are replaced by artificial ones. The artificial tooth is typically attached to the alveolar process by a screw, which requires a screw hole. The orientation and diameter of the screw hole is typically determined from the reconstructed 3D image. The screw hole should be deep enough and in the right angle for a firm attachment. The dislocation of the hole or screw can seriously harm inner organs and cause serious damage to the patient. The CBCT devices can also be applied in other clinical studies related to maxilla facial area, for example ear, nose and throat (ENT) studies, finding tooth fractions or impacted teeth examinations.

Volumetric tomography (VT) is an add-on option for the Orthopantomograph® OP200 dental panoramic device that enables limited angle computed tomography imaging for implant planning in mandibular and maxilla regions [5]. The panoramic device itself is an X-ray device that produces a single and predefined tomographic layer from the dental arc. Therefore, unlike a CBCT study, panoramic imaging can be considered as standard procedure in modern dental care. The VT upgrade

[5]Ortopantomograph is a registered trademark of Instrumentarium Dental, Palodex Group, Tuusula, Finland

consists of a firmware change, dedicated patient positioning system and image processing program embedded into Cliniview^{TM} viewing software in the Windows® environment [6].

The VT scan consists of projection images taken from 45 degree scanning aperture. Since the panoramic X-ray detector is only 6mm wide and the movements of the panoramic device are limited, each of these projection images are taken with a particular scanning movement (see Figure 10). Moreover, accurate imaging geometry for each projection image is determined by adding fiducial reference markers to the bite plate.

The VT has three major benefits compared to dental CBCT devices: Firstly, the cost of VT upgrade is significantly lower than the cost of a CBCT device since there is no need for separate device.

Secondly, the dose is minimal compared to CBCT devices (see the Table on page 2 in the article [II]), since VT uses only up to 11 projection images for the reconstruction while CBCT requires typically hundreds of projection images for the reconstruction. Finally, VT can be installed to any dental office with facilities for a panoramic device and therefore the workflow is simpler.

In the VT procedure, from 5 to 11 X-ray images are taken to gain clinically sufficient cross-sectional slices. After the scan, the projection images are transmitted to a regular workstation where dedicated reconstruction algorithm calculates about 250 slices orthogonal to a dental arc. Moreover, if a panoramic image has been taken using the same bite plate as projection images, the slice position can be associated to the re-projected panoramic layer to gain an orthogonal view along the tooth arc. In practice this means that when viewing the slices in the workstation, also corresponding slice position is indicated from the panoramic image (see Figure 12a). The final diagnosis can then be done based on projection images, orthogonal slices and the panoramic slice. Despite the fact that the panoramic data is not used in the reconstruction process itself, there is an interesting approach by Hyvönen et al(2010) about the usage of the panoramic image as a part of the reconstruction in the VT [7].

The VT approach calls for novel innovations to solve the system-level challenges originated by the limitation of the movements, insufficient and imprecise gantry movements, narrow panel size, anisotropic resolution of the reconstruction and the lack of computational power. To solve these issues, there are three patented innovations related to this product: Firstly, a method for combining linear and rotational movements to produce a virtual focus based imaging geometry [32]. Secondly, a computationally effective iterative reconstruction algorithm [33]. Thirdly, a method for using fiducial markers for defining imaging geometry, slice orientation and combining panoramic images to the slices [34].

Since modifications to the mechanical construction were excluded, the projection images were generated by using standard panoramic detector and panoramic scanning movements. The panoramic device has a 6mm wide vertically oriented detector and two fixed gantry movements; rotational movement around vertical axis and linear movement of the vertical axis towards the column. By a linear movement the rotational axis could be shifted within 60mm distance, while the rotation movement enables at most 200 degree scanning aperture.

[6] CliniView is a common trademark of Instrumentarium Dental, Palodex Group, Tuusula, Finland. Windows is registered trademark of Microsoft Corporation.

The goal of the imaging geometry design was to generate a scanning movement that generates a cone-beam projection, where the X-ray focus point is fixed during the scan and the vertical and horizontal magnification are equal. For that reason, we applied a trajectory for the X-ray source where the virtual focus point could be fixed inside the line intersecting the detector and rotation center and therefore the horizontal magnification could be adjusted and fixed during the scan. The trajectory of the X-ray source is then a cissoid curve, called conchoid. [32]

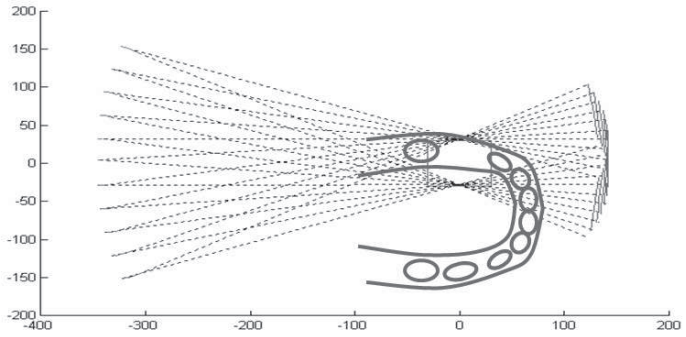

FIGURE 10. Scanning geometry of the VT device. A total of 11 projection images are taken orthogonal to the tooth arc to detect location of the mandibular nerve.

Since movements of the VT device were inaccurate for a reconstruction calculation, reference markers for motion correction were implemented. Since multiple reference steel balls were embedded to the bite plate with beforehand known distance, the imaging geometry could be defined even when only part of the reference markers were visible. Beside defining the actual imaging geometry from the reference markers, the markers could be applied to associate the panoramic slice to the tomographic slices, assuming that the panoramic image has been taken with the same bite plate. Thirdly, the reference markers can be used as a landmark to define the location of the slice, which is convenient especially in the edentulous region. [34]

The most essential innovation in VT was the implementation of the iterative reconstruction in the frequency domain, which is more deeply explained in the patent $US7853056$ [33]. Unlike in spatial domain, in the frequency domain the components that are known based on the imaging geometry can be identified. Then, instead of updating all voxel values, we updated only the frequency components that were located in a limited area. Even though Fourier and inverse Fourier transforms were required during the reconstruction process, the number of floating-point operations was significantly lower than in conventional back-projection and therefore clinically acceptable computational time was gained without any spacial hardware or GPU implementation.

In the VT approach the Fourier slice theorem was directly applied to the cone beam imaging geometry, some compromises had to be made. Fourier slice theorem

as described in the section 2.1.2 cannot be directly used in cone-beam geometry since it assumes that the point spread function (PSF) is constant inside the volume, which is not the case in cone-beam imaging geometry. This could be handled by FDK algorithm as descibed in the Section 2.2.3, but this approach requires workstation with a GPU computing capability and therefore it was not a valid option. Instead, we solved this issue by determining frequency components inside the bow tie shaped region, instead of single line, as shown in the Figure 11. The frequency components that were not included in any projection, were determined by the regularization. More advanced usage of the a priori information was later discovered and described in details in the article [II].

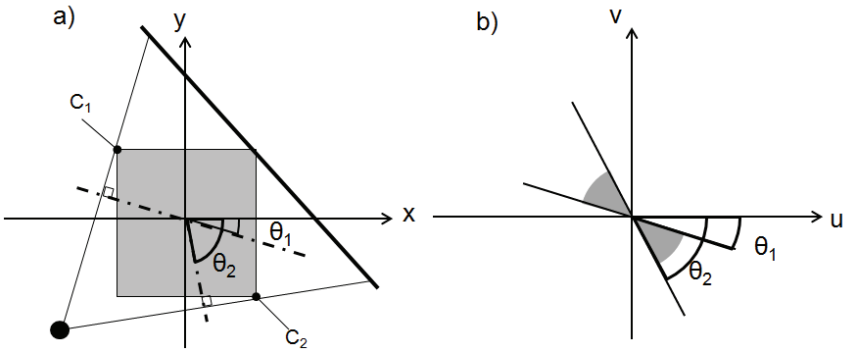

FIGURE 11. The fan beam extension for the Fourier slice theorem used in the VT reconstruction. A single projection image defines the frequency components in a bow-tie shaped region as indicated in the figure b). The opening angle and the orientation of the bow-tie is defined by the corner points (C_1 and C_2) of the field of view (FOV) in the figure a). Unlike the Fourier slice theorem, this approach includes some approximations.

The results from clinical trials of the VT were encouraging. Despite the quantitative imaging quality was better in CBCT device than in VT for obvious reasons, the results indicated that VT can offer similar clinical information in implant planning than CBCT device (as an example, see Figure 12). Moreover, the measuring accuracy was reported to be less than 0.5 mm, which is suitable for the implant planning. Therefore, VT is an illuminating example how limited angle imaging method can successfully replace conventional CT imaging in a clinical operation when dedicated methods are applied.

In the other articles ([II], [III] and [IV]) included in this thesis, several improvements to the VT system are introduced. The Wiener-filter based iterative reconstruction technique (WIRT) and sinogram interpolation technique (SINT) methods described in Sections 3.2 and 3.3 improve the reconstruction image quality and the mutual information based technology (MINT) described in the Section 3.4 improves the accuracy of the imaging geometry. These methods can also be used in any sparse or limited angle X-ray based tomographic device.

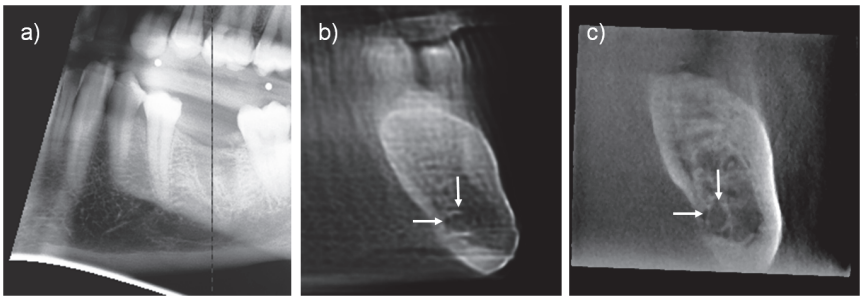

FIGURE 12. a) Panoramic image, where the position of the slice b) is highlighted. Reconstructions taken with a b) VT and c) CBCT device from the same location. The mandibular nerve is highlighted in both images. The VT slice is generated with 11 projection images while in CBCT number of the images is over 300. Regardless of VT slice includes more artifacts, the mandibular nerve is clearly visible in all images.

3.2. **The WIRT method.** The wiener filtered reconstruction technique (WIRT) is a reconstruction method for extremely sparse and limited angle tomography. This method operates in the frequency domain, where the components that require more regularization can be identified and the regularization can be executed only in the regions where less measured information exists or the noise dominates the measured values.

The WIRT method can be divided to following four fundamental steps:

(1) Re-sampling the sinogram
(2) Create the *confidence map*
(3) Primary reconstruction
(4) Optimize the regularization factor

As described in the section 2.4, in typical regularized reconstruction methods each voxel is partly defined by the likelihood and a priori information. The amount of a priori information is defined by the regularization factor (see α in the equation (22)).

Based on the well-known Fourier slice theorem (see Section 2.1.2) each projection image defines the frequency components in a single line. Therefore, in the frequency domain we can define regions where the likelihood should be more accurate since the frequency components are more accurately known than in the regions located away from these lines. Moreover, we can assume that across the projection images the frequency components do not vary significantly, specially in the low frequency region, when the projection angle changes. Obviously this assumption does not hold with every object, but since the object in our case is a real X-ray of a scull, part of the scull or a phantom that simulates the head area, this seems to be the case.

In the WIRT method, we generate a 2D *confidence map*, where each component represents *confidence level* of corresponding frequency component in the reconstruction. Confidence level has a value one when the frequency component of the reconstruction is completely known based on the measurements (i.e. projection images).

Furthermore, the confidence value is linearly decreasing when moving away from the known frequency components (see Figure 2 in the article [II]). In the WIRT method less regularization is applied in the regions where the confidence level is higher and vice versa.

One can also analyze the role of confidence level in the sinogram domain by considering a sinogram consisting few measured columns and estimated sinogram columns between these measured columns. Since the certainty that the interpolated value is correct decreases when the distance form the measured column increases. Therefore, one can also assume that the confidence level also decreases when the distance increases.

Finally, In the confidence map the noise can also be included to the model: If certain projection has relatively more noise than other, the confidence level of noisy projection images can be decreased and more regularization will be applied to that measurement. Therefore, in this method the noise is considered also as uncertainty.

In the WIRT method, we define the optimal reconstruction Ψ in the frequency domain based on the equation

$$\Psi = \underset{\tilde{\Psi}}{\operatorname{argmin}}\left(\left|H\tilde{\Psi} - \Phi\right|_2^2 + \alpha\left|\Gamma\tilde{\Psi}\right|_2^2\right), \tag{24}$$

where $\tilde{\Psi} \in \mathbb{C}^{4N_1N_2}$ is the final reconstruction, $\Phi \in \mathbb{C}^{4N_1N_2}$ is the *primary reconstruction* (i.e. unfiltered back-projection), $H \in \mathbb{C}^{4N_1N_2 \times 4N_1N_2}$ is the frequency response matrix (see equations 3.13 and 3.17 in [II]), $\alpha \in \mathbb{R}$ is the regularization factor and $\Gamma \in \mathbb{C}^{4N_1N_2 \times 4N_1N_2}$ is the confidence map, where $N_{1,2}$ is the size of the reconstruction in the frequency domain (the dimension is multiplied by factor 2 because of the zero-padding).

Solving Ψ from equation (24) leads to

$$\Psi = \left(H^*H + \alpha\Gamma^T\Gamma\right)^{-1}H^*\Phi. \tag{25}$$

Since the H and Γ are diagonal matrices, equation (25) has the element-wise format

$$\psi[\xi_1, \xi_2] = \frac{\overline{\zeta[\xi_1, \xi_2]}}{\left|\zeta[\xi_1, \xi_2]\right|^2 + \alpha(1 - \Upsilon[\xi_1, \xi_2])^2}\omega[\xi_1, \xi_2], \tag{26}$$

where $\zeta[\xi_1, \xi_2]$ is the frequency response of the system (will be explained in detail later in this section), and $\Upsilon[\xi_1, \xi_2]$ is the confidence level in the 2D frequency space spanned by ξ_1 and ξ_2. Here the notation $[\cdot]$ indicates discrete values.

The equation (25) reminds the well-known constrained least square filter (see [21] Section 5.9). However, in the WIRT method, the regularization term is replaced by spatially varying uncertainty in the frequency domain. While in the ART reconstruction (see Section 2.3) the noise could be considered as the residual, in the WIRT method we consider noise as uncertainty.

To define the frequency response, we need to calculate the Fourier transform of the PSF. Generally, PSF is an output of the system when the input is an unit impulse (i.e one in the origin and zero elsewhere). The PSF can be defined either by modeling, by observation or by measuring. In the article [II] we measured the PSF such that we first back-projected the unit impulse and then calculated a Fourier transformation of it. The advantage in using a measured model is that it gives a possibility to accurately model the noise as well.

In the equations (25) and (26) the confidence level defines the relative regularization for each frequency component. The absolute value for the regularization

is defined by the regularization parameter α. Since the regularization parameter has a fundamental effect to the image quality (see Figure 10 in the article [II]), a Newton-Raphson method was implemented to find an optimal value for the regularization parameter that minimizes the total variation of x (see equations 3.24 and 3.25 in [II]).

The WIRT method was numerically implemented in the Octave application GNU/Linux platform. To evaluate the versatility of the WIRT reconstruction, two very different phantoms were chosen: Firstly, Shepp-Logan, since it is a de-facto standard in tomographic articles and secondly a full-scan CT-slice of an dental arc specimen since it indicates the clinical capability of this method. From both phantoms we took 18 projections and added 5% Gaussian noise to the projection images. As references we used ART and SIRT reconstructions by using the same phantoms and imaging geometries, which are known as feasible reconstruction methods for the sparse and limited angle situations. For each algorithm we gave one minute computation time to guarantee fair comparison.

The reconstruction results and metrics indicate that WIRT gives superior result over ART and SIRT especially in the noisy cases and when the results were compared against ground truth (see Figure 13). This result was expected since, unlike in ART and SIRT, in the WIRT method the noise can be modeled and concentrated regularization can be applied.

There are also computationally benefits in the WIRT optimization comparing to the conventional total variation minimizing iterative reconstructions. Firstly, the optimization of the WIRT algorithm can be done in one dimension, which is computationally more effective for obvious reasons. Secondly, small number of dimension enables more robust optimization algorithms that do not require gradient calculations. This is a relevant aspect especially since gradient of the L_1-norm cannot be accurately defined. Finally, since the regularization term has minimal or zero effect to the measured frequency components, there is no need to re-calculate the likelihood values when optimizing the regularization factor.

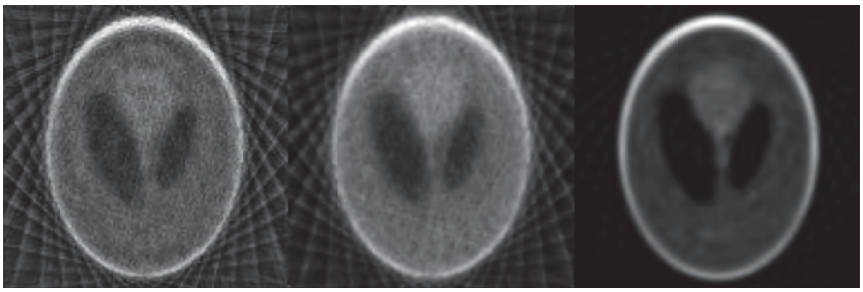

FIGURE 13. Comparison of the Shepp-logan phantom reconstruction results. ART (left) SIRT (middle) and proposed method WIRT (right). In each case, only 18 projection images were used. Originally published in the Article [II]

3.3. **The SINT method.** The SINT (Sinogram Interpolation Technique) is a sinogram interpolation method for extremely sparse tomographic situations. Extremely

sparse here means that only nine projection images around the object were used with 20 degree angular difference between the projection images. In that kind of situation, the non-dedicated interpolation methods fail since the correlation vanishes when the distance from the known sinogram column increases. However, the SINT takes advantage of the characteristics of the underlying sine waves in the sinogram and therefore offers more accurate interpolation resolution. As shortly discussed in the Section 2.1.1, sinogram is a representation of the projection images in an increasing imaging angular order. In this representation, a single point in the volume creates a sine wave to the sinogram where the amplitude of the sine wave equals to the distance between the point and the rotation axis while the wavelength is 2π.

In the article [III] the sinogram is represented as a matrix $S \in \mathbb{R}_+^{N \times H}$, where H is number of projections and N is size of the projection. First we concentrate to estimate a single unknown sinogram column, $S_h \in \mathbb{R}_+^N$ [7]. We define the sinogram as

$$S = [S_1, S_2, S_3, \dots S_{(h-1)}, S_{(h)}, S_{(h+1)} \dots S_{(H-2)}, S_{(H-1)}, S_{(H)}]. \tag{27}$$

The corresponding projection angles are defined as vector $\theta \in \mathbb{R}_+^H$ where $\theta_1 < \theta_2 < \theta_3 \dots \theta_H$. Here all projection angles as well as all sinogram columns excluding S_h are known and fixed.

In the SINT method, grayvalues of the estimated sinogram elements $S_{i,h}$ can be considered as a weighted sum of the adjacent column elements. i.e.:

$$S_{i,h} = \langle w^{(h\pm1,i)}, S_{(h\pm1)} \rangle, \tag{28}$$

where $w^{(h\pm1,i)} \in \mathbb{R}_+^N$ is called the *weight factor vector* related to the sinogram element $S_{i,h}$.

As expressed in equation (28), the grayvalue of a sinogram element $S_{i,h}$ can be determined either based on weighted sum of the sinogram column S_{h-1} or S_{h+1}. In noise-free system both should produce same result since based on the equation 28 $\langle w^{(h-1,i)}, S_{(h-1)} \rangle = \langle w^{(h+1,i)}, S_{(h+1)} \rangle$. However, since we assume that the system includes noise, we use estimation

$$S_{i,h} = \frac{1}{2}\langle w^{(h-1,i)}, S_{(h-1)} \rangle + \frac{1}{2}\langle w^{(h+1,i)}, S_{(h+1)} \rangle, \tag{29}$$

which indicates that the weight factors uniquely define the sinogram value $S_{i,h}$ since the sinogram columns S_{h-1} and S_{h+1} are known.

Another important property of the sinogram is that the sum of the grayvalues in each column is constant. This means in practice that the sum of weight factors per sinogram element has to be exactly one. i.e.:

$$\sum_j w_j^{(h\pm1,i)} = 1 \text{ for each } i. \tag{30}$$

However, these weight factors cannot be directly defined because of the ill-posed nature of the problem.

The purpose of SINT method is to estimate the weight factors w introduced above and then define the missing sinogram column S_h based on that estimation. SINT is based on a novel concept called *warp*, which can be considered as a sum

[7] To simplify the notation, we have used notation S_h to indicate a h:th column of the matrix S. However, to indicate a single element in the sinogram we used standard row, column -order $S_{i,h}$.

of underlying sine waves in the sinogram. Then, the estimated column elements between these two columns can be defined by the grayvalues in the known adjacent columns and the characteristics of the warp. The warps have following essential properties:

(1) Each warp has the shape of a sine wave and a frequency of one.
(2) Each warp connects two sinogram elements in known neighbor columns to a single sinogram element in an estimated column.
(3) Each warp is related to two strictly positive weight factors defined by *warp factor*.
(4) Each warp intersects non-zero sinogram elements in the whole sinogram domain.
(5) All non-zero sinogram elements are associated to at least one warp and all weight factors are associated to exactly one warp.

See also Figure 1.3 in the article [III] for illustration of a warp.

The strategy is to define the S_h by calculating the warp factor vector $\alpha \in \mathbb{R}_+^L$ (where L is the number of warps) mentioned in the item 3 above. Thus, two matrices are generated to connect the warp vector to the grayvalues in the estimated column. Firstly, matrix $G \in \mathbb{R}^{2L \times L}$ is generated to transform the warp factors to the weight factors such that $w = G\alpha$. Secondly, a matrix $A \in \mathbb{R}^{2L \times H}$ is introduced for combining the adjacent columns to the estimated column by weight factors based on the equation (29) such that $S_h = Aw$.

Now the column S_h can be determined by solving the vector α from the equation

$$S_h = AG\alpha \quad \text{such that} \quad RG\alpha = 1, \tag{31}$$

where the matrix $R \in \mathbb{R}^{NN \times 2L}$ implements equation (30).

Since the underlying problem is ill-posed, Tikhonov regularization (see Section 2.4) is used to solve the equation (31). Then the warp vector can be solved from the equation

$$\alpha = ((RG)^T RG + \beta I)^{-1} (RG)^T 1, \tag{32}$$

where β is a regularization parameter. The equation (32) can be solved efficiently by utilizing the singular value decomposition (SVD) of the matrix RG such that $RG = U\Sigma V$. Then

$$\alpha = \sum_n \frac{\sigma_n}{\sigma_n^2 + \beta} v_n. \tag{33}$$

Finally, the regularization parameter β is defined based on the fact that the sum of each sinogram column has to be equal and therefore known also for the estimated column S_h

$$\beta = \underset{\hat{\beta}}{\operatorname{argmin}} \left| \sum S_h^{(\hat{\beta})} - \sum S_{h+1} \right|, \tag{34}$$

which is a small dimensional problem and therefore the optimal value for β can be found by implementing a simple fixed step method.

The method described above gives an estimate for a single sinogram column S_h. When multiple columns are estimated, the matrices introduced in the equation (31) should be generated separately for each estimated column. Then, for each sinogram column, matrices A, G and R have to be separately calculated.

Despite the fact that the SINT method described above is not mathematically thoroughly proved, the preliminary studies indicate that it offers a significantly

better result than non-dedicated interpolation routines and it essentially improves the reconstruction quality in the sparse and noisy situation, which can be observed from the Table 2 and Figures 3,4 and 8. in the article [III]. Moreover, the Figure 2 indicates that the reference interpolation methods are superior to the SINT only when the distance between the estimate and known sinogram columns is relatively small. However, when the distance increases, also the error of the non-dedicated interpolations increases while the error of the SINT method is stable. See also Figure 14 as an example.

The reason for the significantly improved reconstruction quality comparing to conventional interpolation techniques or applying non-interpolated sinogram is that the interpolation routine in SINT method takes account the fact that sinogram consists of rigid sine waves with a fixed wave length. Specially, SINT prevents the warps to intersect the air region and therefore limits the number of the unknown weight factors. Secondly, SINT prefers a solution, where the column sum in the sinogram is constant, which holds specially in noise-free non-local tomography cases.

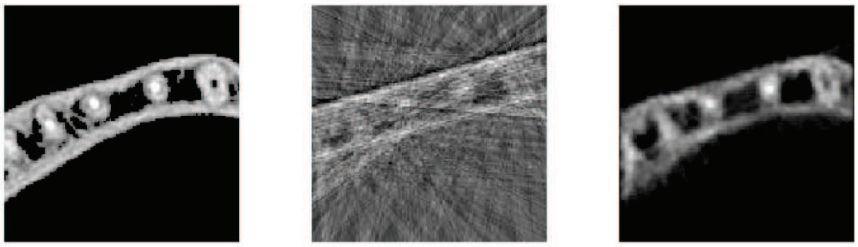

FIGURE 14. Comparison of the FBP and SINT reconstructions of a tooth arc. a) original phantom b) FBP reconstruction and c) proposed SINT method. Nine projection images were used in both reconstructions. Originally published in the Article [III]

3.4. **The MINT method.** The purpose of the MINT is to define the imaging angles of the tomography scan directly from the projection image data without any external markers or angular information. The MINT method utilizes mutual information, which is widely used in medical imaging especially in image fusion [35]. Mutual information is defined as

$$\Upsilon(g_1, g_2) := \sum_{i,j=1}^{N} p(g_1(i), g_2(j)) \log_2 \frac{p(g_1(i), g_2(j))}{p(g_1(i))p(g_2(j))}, \tag{35}$$

where g_1 and g_2 are the grayvalue densities of two images, $p(\cdot, \cdot)$ is the joint probability distribution and $p(g_{1,2})$ are the marginal distribution functions. The advantage of this method comparing to other similar metrics is that re-mapping of the grayvalues (i.e. windowing operation) does not effect the mutual information.

The MINT method consists of four steps:

(1) Filtering the projection images.
(2) Spatially truncating the projection images.
(3) Defining the relative imaging angle.

(4) Defining the absolute angular values.

The first phase generates a phenomenon called *shifting PSF*, which can be described by following simplified demonstration. Let us consider an object that includes a single point with non-zero value, while rest of the object is zero. Then, three affine projections $p_{h-1}(n)$, $p_h(n)$ and $p_{h+1}(n)$ are calculated such that the point is projected to the locations d_{h-1}, d_h and d_{h+1}. The projection images are filtered by Hann filter ψ_f (where f is the length of the filter) and blended as

$$p_b^{\alpha}(n) := (1-\alpha)(\psi_f * p_{h-1}(n)) + \alpha(\psi_f * p_{h+1}(n)), \tag{36}$$

where blending factor $0 < \alpha < 1$. In shifting PSF the maximum peak of the blended projection $p_b(n, \alpha)$ moves from the point d_{h-1} to the point d_{h+1} when α increases. Furthermore, there is a value $\alpha = \hat{\alpha}$ such that $d_h = \underset{n}{\operatorname{argmax}}\, p_b^{\hat{\alpha}}(n)$. Then, also the mutual information between p_h and $p_b(n)$ gains its maximum value (see equation (35)). In the paper [IV] we have shown that the optimal filter size to generate the phenomenon of shifting PSF is $f = 4\,|d_{h-1} - d_{h+1}|$. We also have demonstrated that this idea can be used with more complex projection images.

In the second phase we determine optimal spatial truncation for the projection images based on the acceptable error ε. Then

$$\hat{\theta}_h = (1-\hat{\alpha}_h)\theta_{h-1} + \hat{\alpha}_h\theta_{h+1} + \varepsilon, \tag{37}$$

where θ values are the projection angles.

In the third phase for each projection image h the optimal $\hat{\alpha}_h$ is determined by the biggest mutual information value, i.e.

$$\hat{\alpha}_h = \underset{\alpha}{\operatorname{argmax}}\ \Upsilon\{\tilde{p}_h, \tilde{p}_b^{\alpha}(n)\}, \tag{38}$$

where $\tilde{p_h}$ is filtered and spatially truncated projection image and $\tilde{p}_b^{\alpha}(n)$ is defined in the equation (36).

Finally, the absolute values can be defined from the eigenvalue problem related to eigenvalue one

$$\Gamma\tilde{\theta} = \tilde{\theta}, \tag{39}$$

where $\tilde{\theta} = [\theta_2, \theta_3, \theta_4 \ldots \theta_{M-1}]^T$ and $\Gamma \in \mathbb{R}^{(M-1)\times(M-1)}$ is

(40)

$$\Gamma = \begin{pmatrix} 0 & \hat{\alpha}_2 & 0 & \ldots & \ldots & \ldots & 0 \\ 1-\hat{\alpha}_3 & 0 & \hat{\alpha}_3 & 0 & \ldots & \ldots & 0 \\ 0 & 1-\hat{\alpha}_4 & 0 & \hat{\alpha}_4 & 0 & \ldots & 0 \\ & & & \ddots & & & \\ 0 & \ldots & 0 & 1-\hat{\alpha}_{(M-2)} & 0 & \hat{\alpha}_{(M-2)} & 0 \\ 0 & \ldots & \ldots & 0 & 1-\hat{\alpha}_{(M-1)} & 0 & \hat{\alpha}_{(M-1)} \\ 0 & \ldots & \ldots & \ldots & \ldots & 0 & 1 \end{pmatrix}$$

The matrix Γ in the equation (40) gives a unique solution for the equation (39). Finally, we are ready to determine all angles $\theta \in \mathbb{R}_+^M$ by scaling the angles by known aperture $\theta_M - \theta_1$ and adding the starting angular value θ_1 as follows

$$\theta = \frac{\theta_M - \theta_1}{\tilde{\theta}_{(M-1)}} \begin{pmatrix} 0 \\ \tilde{\theta}(\hat{\alpha}) \end{pmatrix} + \theta_1 \tag{41}$$

where $\tilde{\theta}(\hat{\alpha})$ is the defined by the equation (39).

We also expanded the method to the following situations:

- Fan and cone beam imaging geometry
- Partial volume
- Near full aperture data
- System with a priori angular information

This method was also evaluated by using the VT device introduced in the article [I]. For the evaluation purpose, we randomly selected six clinical cases and removed the reference markers from the projection data to guarantee fair comparison. Moreover, we removed some projection images to gain variability to angular difference and increase the sparsity of the scan. The cone beam and the partial volume extensions were implemented to this method.

The conclusion from this study was that it is possible to estimate the imaging angle from the projection images based on the MINT method described above as indicated in Table 1 in the Article [IV]. Therefore, by implementing this method, basically any X-ray device can be adapted to a sparse or limited angle tomographic device if the scanning aperture is known.

4. Conclusion

In this thesis we have indicated that relevant clinical information for implant planning can be achieved from a small number of projection images taken with a non-dedicated dental X-ray system by applying advanced image processing algorithms. Furthermore, the we have introduced three novel methods to improve the reconstruction quality in this context. Although this approach requires dedicated and more advanced image processing methods and therefore also longer processing times, the benefits are clear: dramatically decreased patient dose, reduced device cost and simplified workflow.

It is also demonstrated in this thesis that besides the reconstruction itself, also pre- and post processing steps play significant role in the reconstruction quality in the limited and sparse tomographic imaging. In particular, the articles [II] and [III] indicate that even when the simple back-projection algorithm was applied, the reconstruction quality could be improved by implementing advanced pre- and post-processing algorithms. Therefore, it is important to consider the reconstruction process as a complete image processing pipeline and optimize each of these phases to gain sufficient reconstruction quality.

One of the key factors of the clinically suitable reconstruction quality is the accurately modeled imaging geometry. This can be achieved either by accurate and repeatable gantry movements or fiducial markers. However, a more practical method to solve this fundamental problem is to estimate the imaging geometry directly form the projection images. In the article [IV] we demonstrated that this is possible with acceptable tolerances in the limited and sparse angle tomography.

Comparing to the full scan CBCT approach, the usage of limited or sparse angle tomography solution in the daily clinical practice requires different workflow and point of view. So far the goal in the CT imaging has been defining the attenuation factors in the individual voxels as accurately as possible by sacrificing the dose, workflow and device cost. In that context, it is obvious that the image quality of the limited or sparse reconstruction is inferior to the full scan reconstruction. However, as indicated in this study, if similar clinical information can be achieved

by using significantly less patient dose, how can one justify the extra dose and extra device cost?

5. Errata

In the article [I], the unit of the DAP (Dose Area Product) was incorrectly defined as $mGycm^{-2}$. The correct unit is $mGycm^2$.

The equation (3.6) in the article [II] should be

$$\Upsilon_{\tilde{\tau}}\left(1-\frac{\Delta\theta\,|\tau|-1}{\Delta\theta\Omega_N-1}\,|\tau-\tilde{\tau}|\right)$$

The equation (3.13) in the article [II] should be

$$\zeta[\xi_1,\xi_2]=\sum_{K=1}^{M}(-1)^{N/2}e^{-i\pi\hat{\xi}}$$

The equation (3.17) in the article [II] should be

$$H=\lceil\zeta(1,1),\zeta(2,1),\ldots,\zeta(2N_1,1),\zeta(1,2),\zeta(2,2),\ldots,\zeta(2N_1,2N_2)\rfloor,$$

The equation on the page 1111 in the article [II] should be

$$\nabla_\Psi F(\Psi)=2H^*H\Psi-2H^*\Phi+2\alpha\Gamma^T\Gamma\Psi,$$

In the Section 4.2 in the article [II], the starting angle of the projection images is 23, not 42. Moreover, in the Section 4.3 the value of N should be 128 instead of 185.

References

[1] J. Hsieh. *Computed Tomography: Principles, Design, Artifacts, and Recent Advances*. SPIE Press, 2009.

[2] Michel M. Ter-Pogossian. *The physical aspects of diagnostic radiology*. Hoeber Medical Division, 1969.

[3] U. Welander. Layer formation in narrow beam rotation radiography. *Acta Radiol. Diagn.*, 16:529–540, 1975.

[4] O. Tokuoka. Layer formation in narrow beam rotation radiography. *Oral Radiology*, 5:31–38, 1989.

[5] Y. Paatero. Pantomography and orthopantomography. *Oral Surg. Oral Med. Oral Pathol.*, 14:947–953, 1961.

[6] Steve Webb. *From the watching of shadows: the origins of radiological tomography*. IOP Publishing Ltd, 1990.

[7] N. Hyvönen, M. Kalke, M. Lassas, H. Setälä, and S. Siltanen. Three-dimensional x-ray imaging using hybrid data collected with a digital panoramic device. *Inverse Problems and Imaging*, 4(2):257–271, 2010.

[8] M. Varjonen. *Three-Dimensional digital breast tomosynthesis in the early diagnosis and detection of breast cancer*. Springer, 2006.

[9] T. Wu, A. Steward, M. Stanto, T. McCauley, and W. Phillips. Tomographic mammography using a limited number of low-dose cone-beam projection mimages. *Medical Physics*, 30(3):385–374, March 2003.

[10] John B. Ludlow, Laura E. Davies-Ludlow, and Stuart C. White. Patient risk related to common dental radiographic examinations. *The Journal of the American Dental Association*, 2008.

[11] John B. Ludlow and Marja Ivanovic. Comparative dosimetry of dental cbct devices and 64-slice ct for oral and maxillofacial radiology. *Oral and maxillofacial radiology*, 2008.

[12] RadiologyInfo.org. Patient safety: Radiation dose in x-ray and ct exams. Technical report, RSNA, 2008.

[13] S. Siltanen, V. Kolehmainen, S. Järvenpää, J.-P. Kaipio, P. Koistinen, M. Lassas, J. Pirttilä, and E. Somersalo. Statistical inversion for x-ray tomography with few radiographs i: General theory. *Physics in Medicine and Biology*, 48:1437–1463, 2003.

[14] V. Kolehmainen, S. Siltanen, S. Järvenpää, J.-P. Kaipio, P. Koistinen, M. Lassas, J Pirttilä, and E. Somersalo. Statistical inversion for medical x-ray tomography with few radiographs: Ii. application to dental radiology. *Physics in Medicine and Biology*, 48:1465–1490, 2003.

[15] V. Kolehmainen, A. Vanne, S. Siltanen, S. Järvenpää, J.-P. Kaipio, M. Lassas, and M. Kalke. Parallelized bayesian inversion for three-dimensional dental x-ray imaging. *IEEE Transactions on Medical Imaging*, 25:218–228, 2006.

[16] R. Pauwels, J. Beinsberger, H. Stamatakis, K. Tsiklakis, A. Walker, H. Bosmans, R. Bogaerts, R. Jacobs, and K. Horner. Comparison of spatial and contrast resolution for cone-beam computed tomography scanners. *Oral and maxillofacial radiology*, 114(1):127–134, July 2012.

[17] D. Rottke, S. Pazelt, P. Poxleitner, and D. Schulze. Effective dose span of ten different cone beam ct devices. *Dentomaxillofacial Radiology*, 42, 2013.

[18] J. Ludlow, L. Davies-Ludlow, S. Brooks, and W. Howerton. Dosimetry of 3 cbct devices for oral and maxillofacial dradiology: Cb mercuray, newtom 3g and icat. *Oral and maxillofacial radiology*, 35:219–226, 2006.

[19] Charles L. Epstein. *Introduction to the Mathematics of Medical Imaging*. SIAM, 2008.

[20] A. C. Kak and M. Slaney. *Principles of Computerized Tomography*. SIAM, 2001.

[21] R. C. Gonzalez and R. E. Woods. *Digital Image Processing (3rd edition)*. Pearson Education inc., 2008.

[22] Anil K. Jain. *Fundamentals of Digital Image Processing*. Prentice-Hall International Editions, 1989.

[23] J. Müller and S. Siltanen. *Linear and Nonlinear Inverse Problems with Practical Applications*. SPIE Press, 2012.

[24] I. A. Feldkamp L. Davies and W. Kress. Practical cone-beam algorithm. *Journal of Optical Society of American*, 1984.

[25] H. Erdogan, G. Gualtieri, and J.A. Fessler. An ordered subsets algorithm for transmission tomography. *IEEE Nuclear Science Symposium and Medical Imaging Conference*, 1998.

[26] H. Erdogan and J.A. Fessler. Monotonic algorithms for transmission tomography. *IEEE Transactions in Medical Imaging*, 18:801–814, 1999.
[27] D. Sowards-Emmerd and L. Shao. Iterative reconstruction for circular cone-beam ctwith an offset flat-panel. *IEEE Nuclear Science Symposium Conference Record (NSS/MIC)*, 2010.
[28] G-H. Chen, J. Tang, and S. Leng. Prior image constrained compressed sensing (piccs): A method to accurately reconstruct dynamic ct images from highly undersampled projection data sets. *Medical Physics*, 25:660–663, 2008.
[29] E. J. Candes and M. B. Wakin. An introduction to compressive sampling. *Signal Processing Magazine, IEEE*, 25(2):21–30, 2008.
[30] J. Kaipio and E. Somersalo. *Statistical and computational inverse problems*. Springer-Verlag, 2005.
[31] A. H. Andersen and A. C. Kak. Simultaneous algebraic reconstruction technique (sart), a superior imlementation of the art algorithm. *Ultrasonic Imaging*, 6:81–94, 1984.
[32] J. Eskelinen. Patent us6990174. Technical report, Instrumentarium Corporation, 2006.
[33] M. Kalke. Patent us7853056 and ep1793347. Technical report, General Electric, 2005.
[34] H. Setälälä. Patent us7499576. Technical report, Palodex Group Oy, 2009.
[35] J. P. W. Pluim, J.B.A. Maintz, and M. A. Viergever. Mutual-information-based registration of medical images: a survey. *Medical Imaging, IEEE Transactions on*, 22(8):986–1004, 2003.

University of Helsinki, P.O. Box 68 FI-00014
E-mail address: martti.kalke@helsinki.fi